Quantifying Flare Combustion Efficiency using an Imaging Fourier Transform Spectrometer

Paule Lapeyre, Rodrigo Brenner, Michael Christopher Nagorski, Jean-Philippe Gagnon, Martin Chamberland, Caroline Turcotte, Kyle J Daun

▶ **To cite this version:**

Paule Lapeyre, Rodrigo Brenner, Michael Christopher Nagorski, Jean-Philippe Gagnon, Martin Chamberland, et al.. Quantifying Flare Combustion Efficiency using an Imaging Fourier Transform Spectrometer. 2024. hal-04418519

HAL Id: hal-04418519
https://hal.science/hal-04418519v1

Preprint submitted on 26 Jan 2024

HAL is a multi-disciplinary open access archive for the deposit and dissemination of scientific research documents, whether they are published or not. The documents may come from teaching and research institutions in France or abroad, or from public or private research centers.

L'archive ouverte pluridisciplinaire **HAL**, est destinée au dépôt et à la diffusion de documents scientifiques de niveau recherche, publiés ou non, émanant des établissements d'enseignement et de recherche français ou étrangers, des laboratoires publics ou privés.

Quantifying Flare Combustion Efficiency using an Imaging Fourier Transform Spectrometer

Paule Lapeyre[1,*], Rodrigo Brenner Miguel[1], Michael Christopher Nagorski[1], Jean-Philippe Gagnon[2], Martin Chamberland[2], Caroline Turcotte[3], Kyle J Daun[1]

[1]Department of Mechanical and Mechatronics Engineering, University of Waterloo
200 University Ave W, Waterloo ON, G2E 6J5, Canada
[2]Telops, Inc. *100-2600 Avenue St Jean Baptiste, Québec QC, Canada*
[3]*Valcartier Research Centre, Defence Research and Development Canada, Québec QC, G3J 1X5, Canada*

Keywords: Hyperspectral Imaging, Flare emissions quantification, Fenceline measurement, Imaging Fourier transform spectrometer, Remote Sensing

*corresponding author.

E-mail address: plapeyre@uwaterloo.ca

Abstract

Mid-wavelength infrared (MWIR) imaging Fourier transform spectrometers (IFTSs) are a promising technology for measuring flare combustion efficiency (CE), defined as the fraction of carbon supplied to the flare as fuel that is converted into carbon dioxide. These devices generate spectrally-resolved intensity images of the flare plume, which may then be used to infer column densities of relevant species along each pixel line-of-sight. In parallel, a 2D projected velocity field may be inferred from the apparent motion of flow features between successive images. Finally, the column densities and velocity field are combined to estimate the mass flow rates for the species needed to calculate the CE. Since the MWIR IFTS can measure all carbon-containing species in the flare plume, it is possible to measure CE without knowing the fuel flow rate, which is important for fenceline measurements.

This work demonstrates this approach on a laboratory heated vent, and then deploys the technique on two working flares: a combustor burning natural gas at a known rate, and a steam-assisted flare at a petrochemical refinery. Analysis of the IFTS data highlights the potential of this approach, but also areas for future development to transform this approach into a reliable technique for quantifying flare CE.

1. Introduction

The petrochemical industry uses flaring to transform high global warming potential (GWP) hydrocarbons (HCs) into CO_2, principally to mitigate the impact of these emissions on climate change. In the case of upstream oil and gas extraction, for example, simple flares are used to dispose of natural gas as a by-product of oil extraction (so-called "associated gas"), while downstream flaring often involves a wider range of hydrocarbon species and more costly and sophisticated flare designs. Globally, 144 billion cubic meters of gas was flared in 2021 [1]. Recovery and reuse processes exist (gas to power, gas to hydrogen, gas reinjection [2]), but their feasibility is subject to favorable economic and technical conditions. Consequently, vast amounts of HCs will continue to be flared for the foreseeable future.

The performance of a flaring process may be quantified by its combustion efficiency (CE), defined as the ratio of the mass flow rate of carbon affixed to carbon dioxide leaving the flare plume to the mass flow rate of carbon affixed to fuel entering the flare stack. While CE is usually assumed to be close to 100% [3], external factors may reduce this number significantly. Crosswinds, for example, can induce an aerodynamic fuel steeping mechanism [4] that removes the fuel from the combustion zone; while steam-assisted and air-assisted flows, which are intended to suppress soot formation, can also cause excess HC emissions [5, 6]. Given the large volumes of HCs flared annually, the impact of flaring on climate change is very sensitive to seemingly small variations on CE. For example, Plant et al. [7] recently determined an average CE for lit flares from upstream processing in Bakken, Eagle Ford, and Permian basins of 95% based on airborne measurements, as opposed to the nominal value of 98% [3]. When unlit flares are considered, the average CE drops to 91%; this 7% difference corresponds to the annual CO_2 emissions of between

2.9-8 million cars [7], with the higher number corresponding to methane having a CO_2(e) of 86 over a 20-year span.

This result highlights the importance of quantifying flare combustion efficiency. *In situ* approaches like extractive gas sampling are viable in laboratory measurements [6, 8] but mostly infeasible on operating flares. A further challenge is that, particularly in the case of fenceline measurements, the fuel flow rate entering the flare is often unknown. Several studies have relied on aerial mass balance measurements by flying an aircraft equipped with gas-analyzers to measure CH_4 and CO_2 concentrations along a helical trajectory surrounding the plume [7, 9, 10]. Species mass fluxes may be obtained by combining concentration measurements with wind speeds, and the fuel supply rate is inferred through a carbon mass balance. While this approach is appropriate for developing an overall sense of flare emissions, e.g., to develop an emissions inventory over a large area, it is not suitable for assessing the performance of individual flares under specific operating conditions.

Accordingly, flare operators, regulators, and equipment manufacturers urgently need diagnostics that can quantify flare CE rapidly through optical standoff measurements. Normal quantitative optical gas imaging (QOGI) cameras are not up to this task, since they cannot distinguish multiple carbon-containing species in the plume. One of the earliest standoff approaches is passive Fourier transform infrared spectroscopy (PFTIR) [11], in which an FTIR is used to measure the spectral intensity emitted by the hot combustion products along a single line-of-sight (LOS) through the plume. A spectroscopic model is then inverted to infer the species concentrations, which are then related to a "local" combustion efficiency averaged along the LOS. A major drawback of this approach is that assumes that the plume is homogeneous in composition,

which is often not the case, and the CE estimate may vary considerably based on the LOS. Consequently, an optical technique that provides both spectral and spatial resolution is desirable.

Zeng et al. [12], adapted a multispectral (MS) camera to visualize the radiant intensity emitted by CO_2, CO, and unburned HCs in the flare plume; the spectral intensity measured by the camera is then related to the relative concentrations of these species through a rudimentary spectroscopic model, providing a local CE for each pixel. Finally, an overall CE for the flare is obtained by averaging the CE for a subset of pixels outside of the combustion zone. While most MS cameras generate images using filter wheels mounted external to the cold shield, these are generally unsuitable for this application since the blackbody emission from the filters dominates the signal component arising from thermal emission by the flare products. Instead, the specialized camera used by Zeng et al. [12] features a microlens array that images the scene onto a number of subdivided regions of the focal plane array (FPA), each of which is equipped with a distinct broadband filter that is cooled along with the FPA. This amounts to a trade-off between spatial and spectral resolution, and typically the number of spectral channels is 10 or smaller. Unfortunately, since the detected spectral intensity is influenced both by species concentration and temperature, it is necessary to measure both these quantities simultaneously, and the number of channels in the MS camera may be inadequate to obtain robust estimates of all the parameters needed to define the gas state within the flare plume.

Mid-wavelength infrared hyperspectral (MWIR-HS) imaging using imaging Fourier transform spectrometers (IFTSs) combine the spectral resolution of PFTIR with the spatial resolution of the MS camera to provide a detailed map of both temperature and species concentration within the flare plume [13]. IFTSs use interferometry to generate a data cube of thousands of near-simultaneous images, leading to a spectral resolution that far exceeds what is possible using a MS

camera without sacrificing spatial resolution, although at the expense of temporal resolution. The spectroscopic data may be inverted to solve for the temperature and species concentration fields simultaneously; these concentrations are then combined with a 2D map of intensity-weighted velocities inferred from a sequence of raw broadband images in the interferogram to produce mass flow rates.

This instrument has been used to measure gaseous emissions from a variety of industrial combustion processes, including smoke stacks [14] and engine exhausts [15]. In the context of emissions monitoring, key advantages of this approach include: (1) the spectral and spatial resolution is generally sufficient to obtain the concentration and temperature gradients, which are important in heterogenous plumes; (2) the spectral resolution may be further used to fingerprint species when the plume has an uncertain chemical composition; and, in the case of emission spectroscopy, (3) measurements may be carried out in day or night, and are not as sensitive to nonuniform background illumination as are techniques based on absorption spectroscopy, e.g., using the sun or a cloud layer.

Savary et al. [16] were the first to use IFTSs to infer flare CE. In their work, the plume temperature and species concentrations are assumed to be homogeneous along each LOS in order to simplify the spectroscopic model. However, Grauer et al. [17] and Miguel et al. [18] used CFD simulations to demonstrate that Gaussian distributions are more appropriate in the case of flare plumes. Miguel et al. [18] also conducted several proof-of-concept measurements on lab scale heated vents and a lab-scale steam and air-assist flare.

This work applies the technique developed by Grauer et al. [17] and Miguel et al. [18] to conduct benchmarking experiments on a heated vent under conditions representative of a flare plume, and then measure the combustion efficiency of a portable combustor (enclosed flare)

operating at as known firing rate and a steam-assisted flare at an oil refinery burning an unspecified fuel at an unknown rate. In the case of the combustor, the carbon mass flow rate in the plume is consistent with the estimated fuel supply rate, and the overall combustion efficiency is nearly 100%. The refinery flare, in contrast, is over-assisted and a significant quantity of unburned hydrocarbons are visible in the plume. The paper concludes with an assessment of the strengths and weaknesses of this approach, and areas for improvement. In particular, while the IFTS provides rich spectral data, a major challenge concerns the inference procedure and the model errors that are made to reduce the ill-posed problem. Overall, however, these results highlight the promise of this technique, and its potential to reduce greenhouse gas emissions from flaring.

2. Flare combustion efficiency

Flare combustion efficiency is defined as the mass flow rate of the carbon affixed to CO_2 leaving the flare plume divided by the mass flow rate of carbon entering the flare stack. Since the latter quantity may not be readily available, particularly for fenceline monitoring, it may instead be inferred from a mass balance of all carbon-containing species in the flare plume

$$\mathrm{CE} = \frac{\dot{m}_{\mathrm{C,CO_2}}}{\dot{m}_{\mathrm{C,fuel}}} \approx \frac{\dot{m}_{\mathrm{C,CO_2}}}{\sum \dot{m}_{\mathrm{C,plume}}} \tag{1}$$

As shown in Figure 1, the mass flow rate of the *k*th species in the plume is found by integrating the product of the corresponding species column density (kg/m^2) with the normal component of the 2D projected velocity along a control line that transects the plume in the image plane

$$\dot{m}_{\mathrm{C},k} = \frac{M_{\mathrm{C}}}{M_k}\dot{m}_k = \frac{M_{\mathrm{C}}}{M_k}\int_{\Theta} \rho_k(\theta)\,\mathbf{u}(\theta)\cdot\hat{\mathbf{n}}\,d\theta \tag{2}$$

where the mass flow rate is adjusted by the ratio of the carbon molar mass, M_C = 12 atomic mass units (amu), and the kth species molecular molar mass, M_k, to obtain the mass flow rates of carbon. The pixel column density of the kth species for the LOS at a location θ along the control line is

$$\rho_k(\theta) = \frac{M_k p}{k_B N_A} \int_{\mathrm{LOS}(\theta)} \frac{\chi_k(s,\theta)}{T(s,\theta)} ds \tag{3}$$

where p is the atmospheric pressure, k_B is Boltzmann's constant, N_A is Avogadro's number, and $T(s,\theta)$ and $\chi_k(s,\theta)$ are the temperature and mole fraction of the kth species evaluated at a location s along an LOS for a pixel located at θ on the control line. The procedures for calculating the species concentration, the plume temperature and the projected velocity field are described in the Sec. 4. In principle the denominator of Eq. (1) could include soot, although the contribution of soot to the overall carbon balance is usually negligible [19].

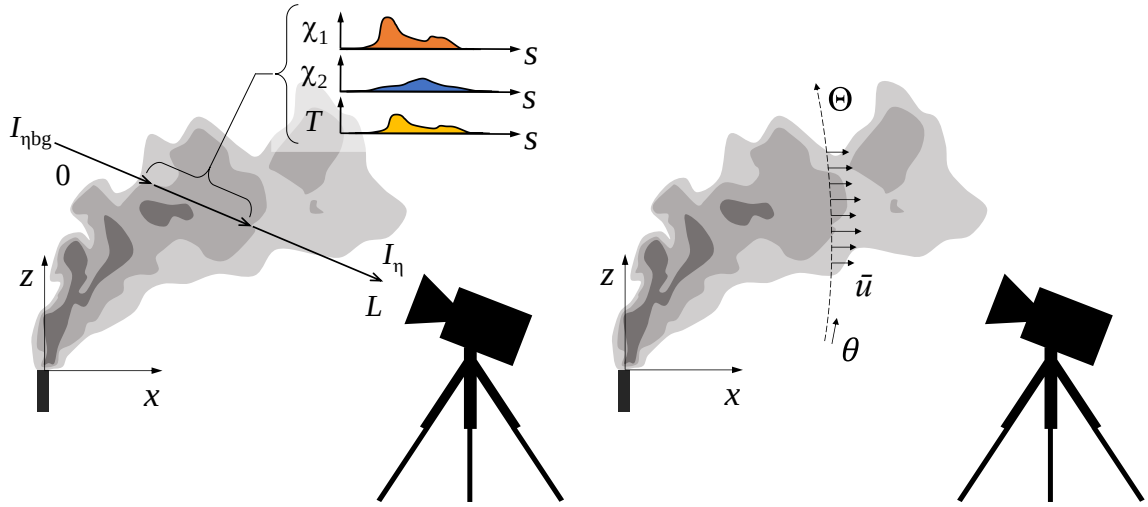

(a) (b)

Figure 1: Schematic of a flare combustion efficiency measurement using an IFTS: (a) temperature and species concentration distributions are inferred from a spectroscopic model, Eq. (4); (b) these distributions are then used to derive column densities along a control line through Eq. (3), which is combined with a 2D intensity-weighted velocity map to obtain mass flow rates via Eq. (2).

3. Measurement model

The measurement model connects the quantities-of-interest, in this case the temperature and concentration distribution along each line of sight within the plume, to the spectral intensity measured by the IFTS. It is composed of a spectroscopic model, describing the intensity emitted by the scene that is incoming to the camera aperture, and a camera response model, describing the effect of the instrument on the incident scene intensity.

3.1. Spectroscopic model

The spectral intensity at wavenumber η entering the camera aperture, $I_{\eta,L}$, is defined by the radiative transfer equation (RTE) along each pixel line-of-sight

$$I_{\eta,L} = I_{\eta,\mathrm{bg}} \exp\left(-\int_0^L \kappa_\eta(s)\, ds \right) + \int_0^L \kappa_\eta(s) I_{\eta,\mathrm{b}}\left[T(s)\right] \exp\left(-\int_s^L \kappa_\eta(s')\, ds' \right) ds \tag{4}$$

where L is the length of line-of-sight from behind the plume to the camera aperture, $I_{\eta,\mathrm{bg}}$ is the background intensity, $I_{\eta,\mathrm{b}}$ is the blackbody intensity, and κ_η is the spectral absorption coefficient.

The background intensity may be determined from a pixel outside of the flare plume, although its contribution to $I_{\eta,L}$ is usually small compared to the emission term over the vibrational-rotational (V-R) bands of the species in the plume. For N_s participating species (e.g., CO_2, CO, H_2O, and various HCs) the spectral absorption coefficient is given by

$$\kappa_\eta(s) = \sum_{k=1}^{N_s} \kappa_{\eta,k}\left[\chi_k(s), T(s)\right] \tag{5}$$

The spectral absorption cross-sections of individual species may be found using a spectral line database (e.g. HITRAN [20]) or from empirical spectra. In the case of HITRAN-derived spectra,

157 the absorption coefficients of common species are precomputed for given concentrations and
158 temperatures, assuming air broadening:

159 $$\kappa_{\eta,k}\left[\chi_k(s),T(s)\right]=\sum_{ij}S_{k,ij}\left[T(s)\right]f\left[\eta,\eta_{ij},T(s),p\right]\frac{\chi_k(s)p}{k_{\mathrm{B}}T(s)} \quad (6)$$

160 where $S_{k,ij}$ is the species spectral line intensity for the transition between the *i*th and *j*th energy
161 states, and f is the Lorentz line shape function. (Doppler broadening is negligible at the
162 temperatures and pressures relevant to flare plumes.)
163
164 *3.2.Camera response model*
165 Hyperspectral imaging is done using a Telops MW HyperCam IFTS with a detection spectrum of
166 1900-3400 cm^{-1}, which includes V-R bands of CO_2, H_2O, CO, and most HCs, and a maximum
167 spectral resolution of 0.25 cm^{-1}. The focal plane array (FPA) is composed of 320×256 pixels with
168 an instantaneous field-of-view (IFOV) of 0.35 mrad per pixel. The FPA is made of InSb sensors,
169 which records the interferogram image generated by a Michelson interferometer as shown in Figure
170 2 (*a*). As the moving mirror move across its range, an interferogram Y_{cam} is formed, as shown in
171 Figure 2 (*b*). The mirror position defines the optical path difference (OPD), which characterizes the
172 difference in pathlengths travelled by the two light beams generated by the beam-splitter. The beams
173 are then recombined, generating interferences that are measured by the FPA to form an interferogram.
174 A Fourier transform is performed on the interferogram in counts to obtain an intensity spectrum with
175 arbitrary units. Finally, an absolute intensity spectrum is obtained by calibrating using a two-point
176 calibration method [21] using two built-in blackbodies maintained at different temperatures.
177 The IFTS camera response model, referred to as the instrument line shape (ILS) function,
178 relates the scene intensity entering the camera aperture $I_{\eta,L}$ to the measured intensity, and describes

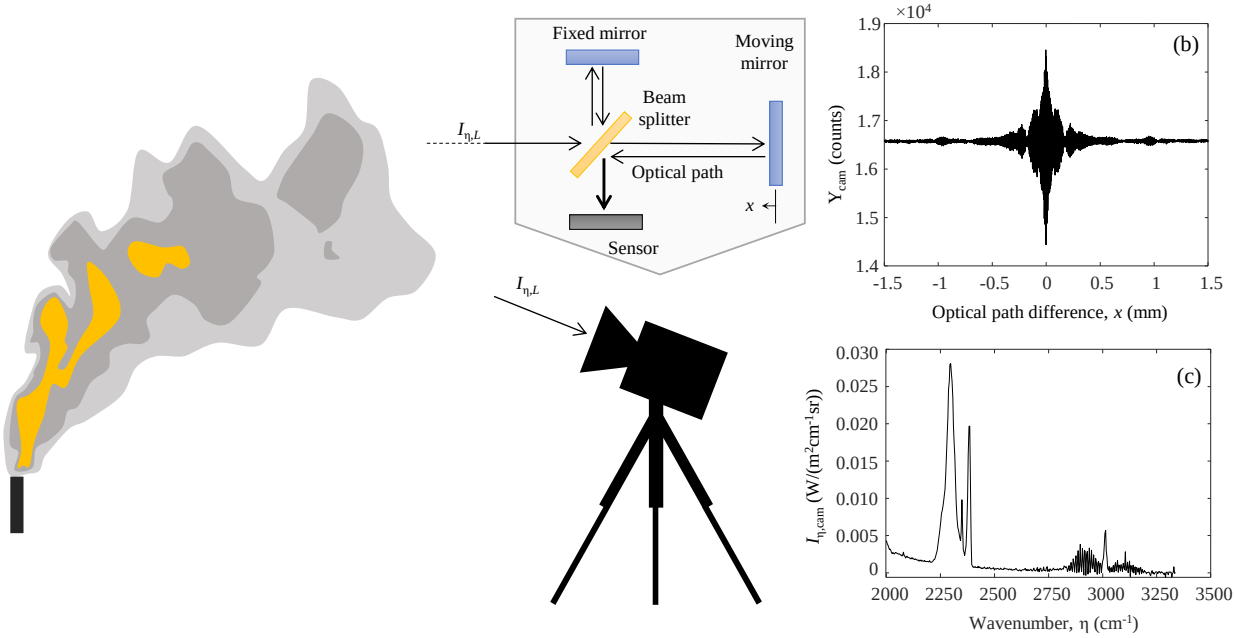

Figure 2: IFTS measurement process. (*a*) The scene radiation $I_{\eta,L}$ enters the camera aperture and traverses the Michelson interferometer, generating interferences measured by the FPA InSb sensors for successive mirror position. (*b*) The measured raw signal is the interferogram Y_{cam}. Finally, (*c*) the interferogram is Fourier transformed and calibrated by a two-point calibration method to produce the absolute intensity spectra $I_{\eta,cam}$.

how the IFTS mirror position limited range affects the measurement. In theory, the interferogram $Y_m(x)$ is defined for $x \in \mathbb{R}$. However, the range of the moving mirror in the camera is limited to a maximum OPD, x_{MOPD}, which is related to the spectral resolution by $\delta\eta_{res}=1.20671/2x_{MOPD}$. The measurement model accounts for the finite range of the mirror and relates the intensity $I_{\eta,L}$ to the modelled measurement, $I_{\eta,m}$, by the convolution product:

$$I_{\eta,m} = \mathcal{F}\left[Y_m(x)\, B(x, x_{MOPD})\right] = \mathcal{F}\left[Y_m(x)\right] * \mathcal{F}\left[B(x, x_{MOPD})\right] = I_{\eta,L} * ILS(\eta, x_{MOPD}) \qquad (7)$$

where B is the boxcar function that characterized the finite OPD and becomes the ILS when the Fourier transformation is applied. Modelling the measured intensity then comes down to a convolution product between the intensity spectra, given by Eq. (4), and the ILS, which is $ILS(\eta,x_{MOPD}) = 2x_{max}\mathrm{sinc}(2\pi x_{MOPD}\cdot\eta)$.

One of the challenges inherent to hyperspectral measurements of turbulent flows are rapid variations in intensity caused by fluctuations in the species concentration and temperature, which occur over a much shorter time scale than the time needed for the mirror to traverse its entire OPD range. These intensity fluctuations manifest as "scene change artifacts" (SCAs) in the transformed intensity spectrum [15]. Indeed, the interferogram model assumes that the intensity field remains constant as the interferogram is assembled:

$$Y_{\mathrm{cam}}(x) = \int_{-\infty}^{+\infty} \frac{1}{2} S_{\eta} \left[1 + \cos\left(2\pi\eta x\right) \right] d\eta \tag{8}$$

where S_η is the intensity entering the interferometer, representing the scene intensity $I_{\eta,L}$ and the camera self emission. The turbulent fluctuations of the flare plumes are expressed in Eq. (8) through the time dependence of the intensity field $S_\eta \equiv S_\eta(t)$. Following the hypothesis that the true intensity field is stationary but fluctuating, SCAs may be suppressed by using a high band pass filter to isolate the low frequency intensity variations, Fig. 3 (*a*), and then removing them from the

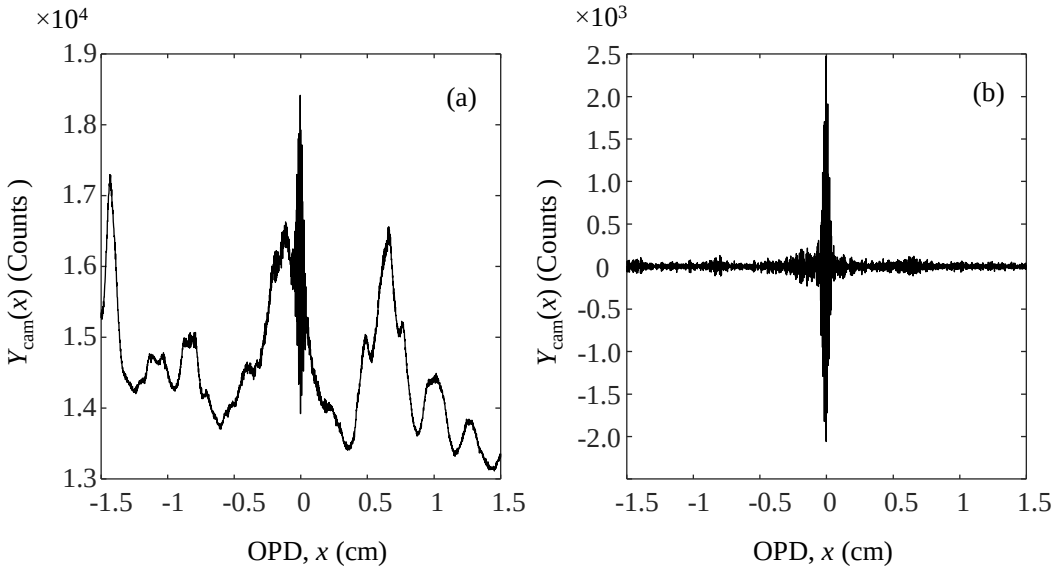

Figure 3: The raw interferograms $Y_{\mathrm{cam}}(x)$ (a) are contaminated by scene change artifacts caused by turbulent fluctuations in the flow field as the mirror traverses through its OPD. These can be removed through a filtering procedure (b).

measured interferogram to obtain a new filtered interferogram, Fig. 3 (*b*). The filtered raw spectrum *Y*, cleared from the intensity fluctuations, is then transformed to obtain a raw intensity spectrum, S_η. An alternative approach, used in this work, consists of estimating a median interferogram from a large set of raw datacubes.

4. Inferring the mass flow rates

Calculating the species mass flow rates from Eq. (2) relies on solving the column densities and the projected velocity profile along the control line. The column densities are obtained from the species mole fractions and plume temperature distributions along the LOS of each pixel on the control line; these quantities, in turn, are found by inverting the spectroscopic measurement model. The image projected velocity field is found from the apparent motion of pixels between sequential broadband images.

4.1.Inferring the mole fractions and plume temperature

Inferring the species mole fractions and the temperature profiles along a pixel LOS amounts to minimizing the residual between the measured and modeled spectral intensities for each LOS. This inversion problem is mathematically ill-posed since an infinite combination of $\chi_k(s)$ and $T(s)$ could be substituted into Eq. (4) to generate a given spectral intensity. Accordingly, it is necessary to parameterize the distributions along the pixel LOS to reduce the ill-posedness of the problem. Following the work of Miguel et al. [18], and Grauer et al. [17], we assume Gaussian profiles inside the plume along the LOS, which are appropriate for free turbulent plumes, and constant values for the atmospheric layer between the plume and the camera aperture:

$$\phi(s) = \phi_{\text{amb}} + (\phi_{\text{max}} - \phi_{\text{amb}}) \exp\left[-\frac{(s - s_{\text{pc}})^2}{2\sigma_{\text{p}}^2} \right] \tag{9}$$

where $\phi = \chi_k$ or T, σ_{p} is the characteristic plume thickness, and s_{pc} is the location of the plume center. The ambient concentrations and temperature may be derived from meteorological data, or determined by examining the spectra from a pixel outside of the flare plume, e.g., the flare stack. The plume thickness is assumed to be the same for all parameters and is estimated from the plume image, assuming that the plume is axisymmetric. The plume center is determined by the measured distance between the camera and the flare stack. Therefore, the number of unknown parameters to be solved for is $N_{\text{s}}+1$, corresponding of the peak concentration of each species and the peak temperature; these are stored in the vector **x**. The maximum likelihood estimate is then found for each pixel/LOS by

$$\mathbf{x}_{\text{MLE}} = \arg\min_{\mathbf{x}} \left\{ \left[\mathbf{m}(\mathbf{x}) - \mathbf{b} \right]^{\text{T}} \boldsymbol{\Gamma}_{\text{b}}^{-1} \left[\mathbf{m}(\mathbf{x}) - \mathbf{b} \right] \right\} \tag{10}$$

where **m** is the measurement model, defined in Sec. 2, **b** contains the set of spectral intensities at each wavelength $\{I_{\eta,\text{cam}}\}$, and $\boldsymbol{\Gamma}_{\text{b}}$ is the measurement error covariance matrix, which is assumed to be diagonal and is computed from the measurement variance for each IFTS spectral bin. Minimization is carried out using the nonlinear least-squares solver in MATLAB® with a function tolerance of 10^{-9} and a step tolerance of 10^{-9} [22]. In some cases, the spectral range of the data is restricted to a subset of the detection spectrum that contains species-of-interest, in order to reduce computational time and exclude features that are not included in the model, such as background intensity from the atmosphere.

4.2.Inferring the velocity field

The time-resolved 2D velocity field, $\mathbf{u} = [u, v]^T$, is derived from a set of successive raw interferometer images via either the Horn-Schunk [23] or Lucas-Kanade optical flow algorithms [24]. The intensity of each image is first normalized and the mean pixel intensity field is subtracted to remove the stationary features. Optical flow is based on the hypothesis that any change in pixel brightness between successive images is due entirely to advection. Accordingly, pixel intensity becomes a conserved quantity and the velocity field is obtained by solving

$$\frac{DE}{DT} = \frac{\partial E}{\partial x}u + \frac{\partial E}{\partial y}v + \frac{\partial E}{\partial t} = 0 \tag{11}$$

where E is the modified broadband pixel intensity and the derivatives are found from finite difference approximations. Solving for the 2D velocity field requires additional information to close the problem. In the Horn-Schunk algorithm, this is done by assuming that the velocity components vary smoothly in space, which correspond to Tikhonov first-order regulation:

$$\begin{cases} \nabla^2 u = \dfrac{\partial^2 u}{\partial x^2} + \dfrac{\partial^2 u}{\partial y^2} \\ \nabla^2 v = \dfrac{\partial^2 v}{\partial x^2} + \dfrac{\partial^2 v}{\partial y^2} \end{cases} \tag{12}$$

The Lucas-Kanade algorithm adopts a weighted window scheme to filter the velocity field calculation, thereby suppressing noise amplification by the numerical derivative. In that case, the weighting term is the equivalent to first-order Tikhonov regularization. The regularization parameters are usually chosen heuristically, as is done here.

5. Experimental analysis

The technique is demonstrated by conducting measurements on a laboratory-scale heated vent, combustor, and a steam-assisted petrochemical flare.

5.1.Laboratory-scale heated vent

The performance of this technique is first benchmarked using the heated vent apparatus shown in Figure 4 (*a*), consisting of a 1.9 cm diameter nozzle positioned in front of four aluminum plates (30 cm × 30 cm each), coated with matte black paint (Krylon k01602 Ultra-flat black) and maintained at a set-point temperature of 281 K by a water/ethylene glycol mixture. A specified 47:53 vol. mixture of CH_4 (53%) and CO_2 (47%) is generated using mass flow controllers (Brooks SLA5850 for CO_2 and Brooks GF40 for CH_4) at a total flow rate of 25.5 standard litres per minute

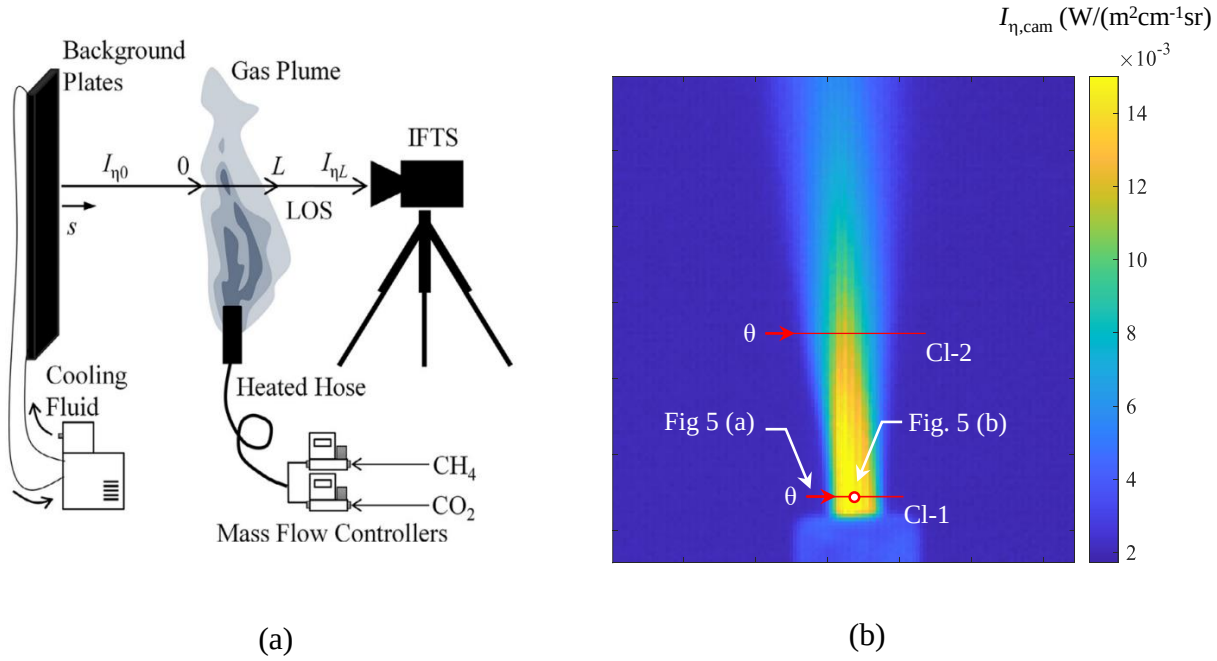

(a) (b)

Figure 4: (*a*) laboratory scale apparatus, the hyperspectral camera is aiming at the gas plume. (*b*) The camera generates infrared images of the emitted radiation from the plume. The analysis is conducted over two control lines, Cl-1 near the stack exit and Cl-2 located 6.6 cm above the stack exit.

(SLPM). The gas mixture then flows through a heated hose before it is discharged from the nozzle. The gas temperature is maintained at 350 K via a K-type thermocouple located at the nozzle exit.

Hyperspectral measurements were conducted with the camera aperture located 420 cm away from the plume, using a 128 px ×128 px subdomain of the FPA. The detection spectrum was set between 1,900 cm^{-1} and $3{,}400^{-1}$ with a spectral resolution of 4 cm^{-1} and a fixed integration time of 100 μ s. However, during the inference, only a subset of the spectrum was used, containing the species-of-interests absorption spectral ranges, from 2200 to 2470 cm^{-1} for CO_2 and from 2800 to 3300 cm^{-1} for CH_4. The ambient CO_2 concentration was assumed to be 420 ppm and the temperature of the atmospheric layer between the plume and the camera was measured at 295 K. Inferring the ambient temperature from background pixels led to T_{amb} = 297 K, which is in good agreement with the measurement.

The control line Cl-1was positioned near the stack exit, as shown in Figure 4 (*b*), so the gas velocities could be estimated from the known mass flow rates and nozzle dimensions. Because the control line is located above the stack exit, the velocity and concentration profiles are assumed to be uniform along the control line region covering the stack nozzle. The absence of turbulent flow features at the nozzle exit precludes calculating the gas velocity from optical flow, so the gas exit velocity is estimated to be 1.5 m/s from the known mass flow rate and the nozzle diameter. Therefore, calculating the mass flow rate at this position provides a means to isolate how uncertainty in the spectroscopic model impacts the mass flow rate.

Figure 5 (*a*) shows the column density profiles for CO_2 and CH_4, as well as the inferred plume temperature for the control line “CL-1” in Fig. 4 (*b*). The inferred ambient temperature (297 K) was used for this calculation. The plume temperature inferred from the IFTS data is around 400 K instead of the measured 350 K at the stack exit. The column density profiles of CO_2 and CH_4 show

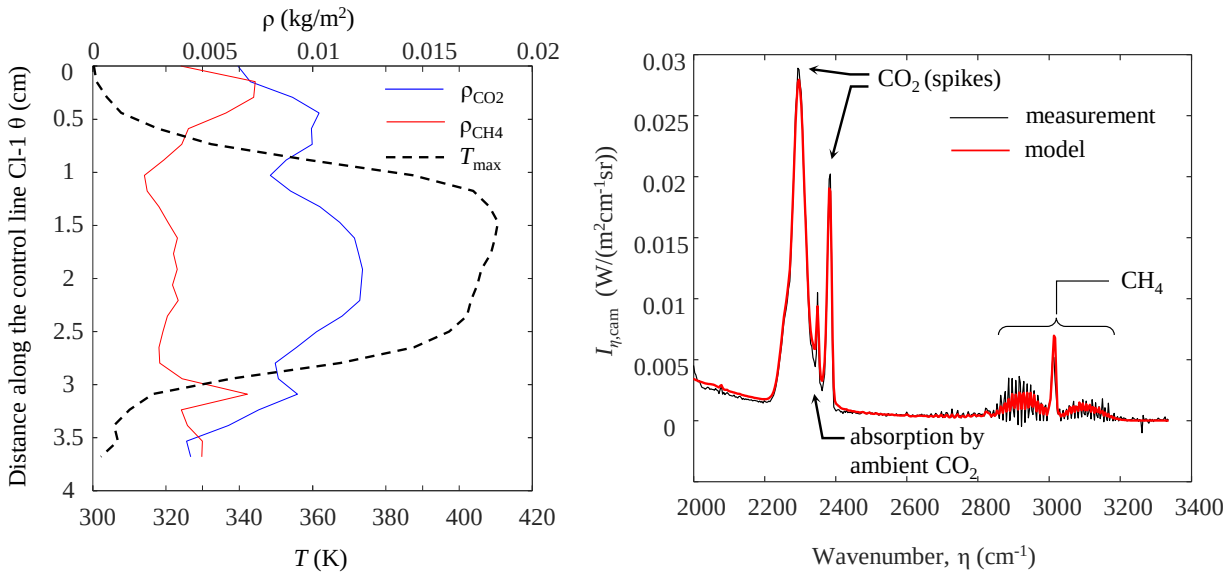

Figure 5: (*a*) Column densities and temperatures inferred from the IFTS camera data for the integration line Cl-1 shown in Fig. 4 (*b*). (*b*) Comparison of modeled and measured spectra at the pixel location shown in Fig. 4 (*b*).

spikes at the extremities of the control line, which is due to the fact that the contribution of thermal emission from the gases to the detected intensities is small at this location, and the inference becomes dominated by measurement noise and model error. Since the values do not cover the plume, they are excluded from the mass flow rate estimations, which is conducted from θ = 0.7 cm to θ = 2.9 cm. Figure 5 (*b*) shows that the modeled spectrum at the sample point indicated in Fig. 4 (*b*) closely matches the measured intensity. Features for both CO_2 and CH_4 are visible at 2,200-2,400 cm^{-1} and 2,800-3,200 cm^{-1}, respectively. The measured emission spectra from the plume reveals two CO_2 emission "spikes" at 2,250 ("red spike") and 2,400 cm^{-1} ("blue spike"). This feature arises from the fact that a portion of emission from 001 fundamental CO_2 band in the plume is absorbed by the ambient CO_2 between the plume and the camera, only leaving the hot lines at the wings of the band.

306 The control line Cl-2 was positioned 6.6 cm above the stack exit, as shown in Figure 4 (*b*), so
307 the gas velocities are inferred from the Horn-Schunk optical flow algorithm. Gaussian profiles for
308 the plume concentrations and temperature are assumed due to the turbulent nature of the plume at
309 that location (see Eq. (9)). The inferred column density profile for CO_2 and CH_4 are shown in
310 Figure 6 (*a*), as well as the maximum temperature distribution along Cl-2. Figure 6 (*b*) shows the
311 corresponding velocity profile used to estimate CO_2 and CH_4 mass flow rates. The mass flow rates
312 are computed from $\theta = 0.6$ cm to $\theta = 5$ cm to exclude the background pixels from the mass flow
313 rate calculation.

314 Table 1 shows that the inferred mass flow rate for CO_2 and CH_4, along Cl-1 and Cl-2, are in
315 good agreement with the mass flow controller settings.

316 Table 1: CO_2 and CH_4 carbon mass flow rates inferred from the heated vent.

	IFTS (Cl-1)	IFTS (Cl-2)	MFC	% diff. (Cl-1)	% diff. (Cl-2)
$\dot{m}_{C,CO2}$ ($\times 10^2$ g/s)	8.9	8.4	8.37	5.9	0.3
$\dot{m}_{C,CH4}$ ($\times 10^2$ g/s)	8.1	9.6	9.45	-13.9	1.6

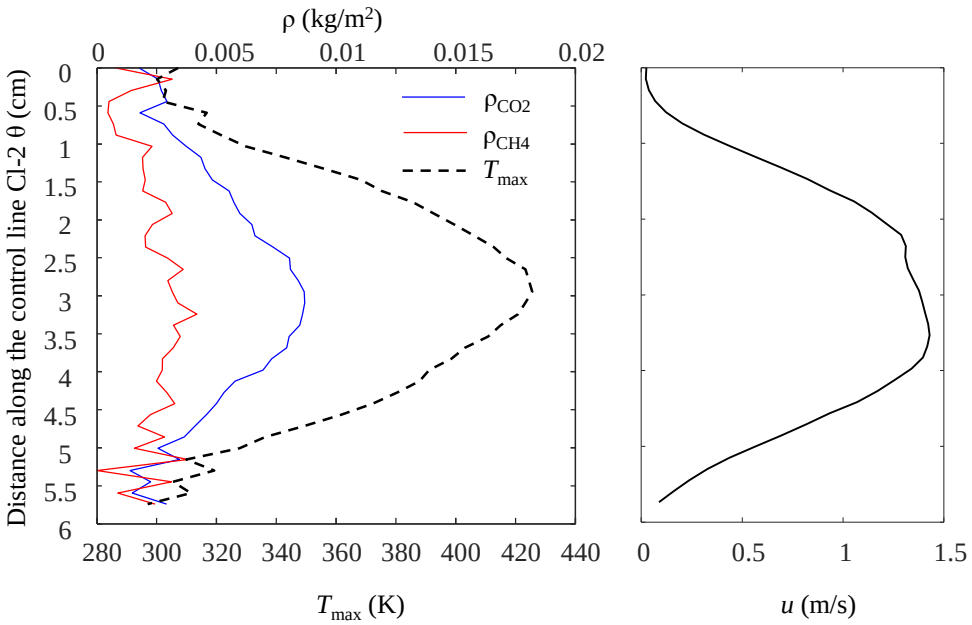

Figure 6: (*a*) Column densities and temperatures inferred from the IFTS camera data for the integration line Cl-2 shown in Fig. 4 (*b*). (*b*) Velocity profile inferred from the Horn-Schunk optical flow algorithm.

317

318

5.2. IFTS measurement of a combustor

Figure 7 (*a*) shows a Questor Q100 combustor that was operated at Carbon Management Canada's Newall County Research Station. The combustor was supplied with natural gas (~94.2% CH_4, 3.4% C_2H_6, 1.1% C_3H_8, and 1.3% minor components by volume) at approximately 42.5 standard cubic meters per hour. Local meteorological conditions (windspeed, wind direction, and temperature) were measured by a Davis onsite weather station, while ambient CO_2, CH_4, and H_2O concentrations were measured by a Picarro cavity ringdown spectrometer.

Figure 7 (*b*) shows the spectral intensity map at $\eta = 2283$ cm^{-1}, corresponding to the CO_2 "red spike." Measurements were conducted at a distance of 150 m from the combustor stack exit, using a 128 px×128 px subdomain of the FPA, corresponding to a (6.6×6.6) m^2 area of the scene. The detection spectrum was set between 1900 cm^{-1} and 3400 $^{-1}$ with a spectral resolution of 4 cm^{-1} and a fixed integration time of 50 μs. Figure 8 shows the intensity spectra for pixels "A" above, "B" within, and "C" beneath the plume, along with the absorption coefficients of species that may be in the plume (H_2O, CO, CO_2, CH_4). The spectra for pixels "A" and "B" show blackbody-like behavior at low wavenumbers corresponding to an average temperature of approximately 255 K under clear conditions. As one would expect, the spectral intensity for the plume pixel "B" is much larger than those of "A" and "C" due to the thermal emission of the hot species. The intensity spectra indicate the presence of CO_2, H_2O, CO, but shows no detectable CH_4, suggesting that the combustor is operating with a high CE. Note also that the red and blue CO_2 spikes are more pronounced compared to Fig. 5, due to the greater column density of ambient CO_2 between the camera and the plume.

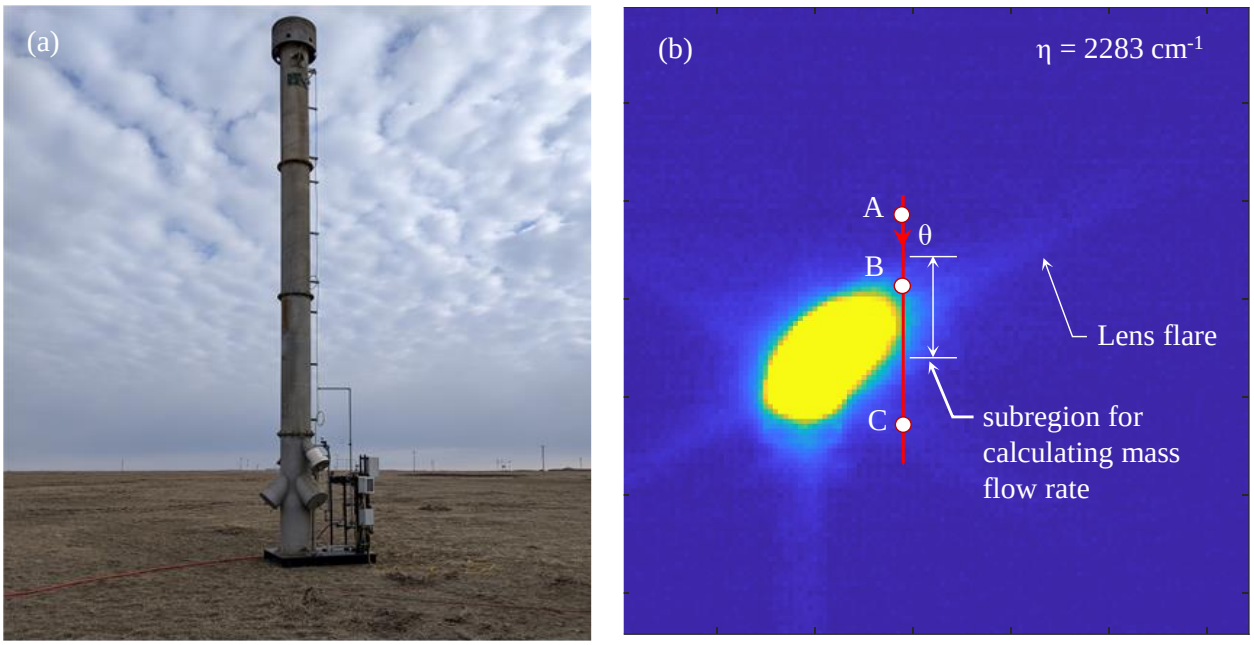

Figure 7: (a) Questor Q100 combustor; and (b) the intensity map at η = 2283 cm^{-1}, corresponding to the CO2 red spike. Spectra for locations A, B, and C along the integration line are shown in Fig. 8. Lens flare artifacts extend diagonally from the region of peak intensity.

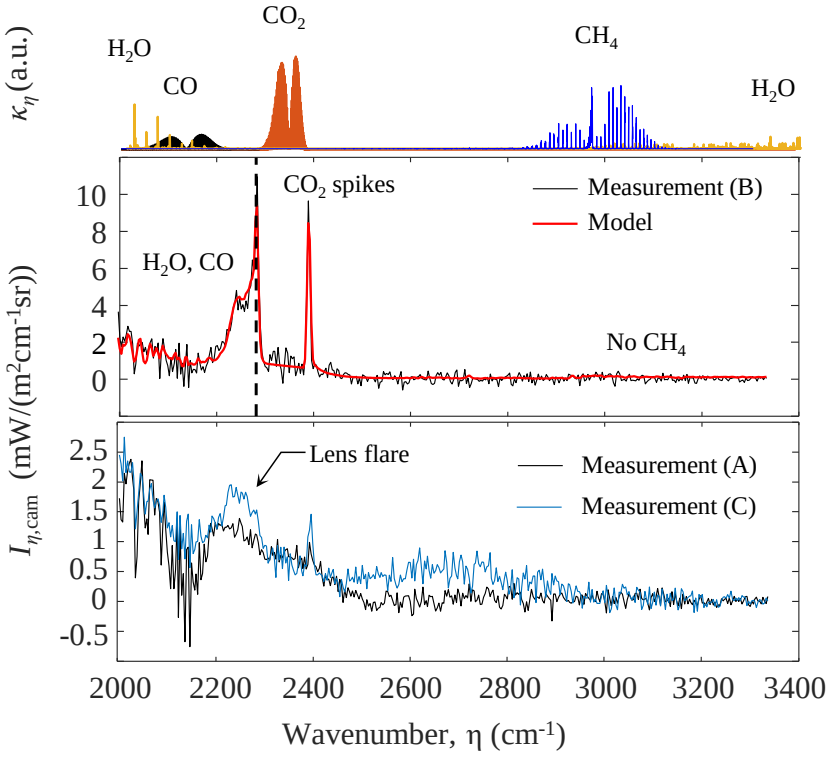

Figure 8: Spectra for pixels “A”, “B”, and “C” shown in Fig. 7. Note the difference in scale between the top and the bottom plots.

The infrared intensity map in Fig. 7 (b) also reveals lens flare artifacts, which extend diagonally from the brightest spot on the image. These artifacts affect all of the broadband images used to construct the interferogram, and are therefore difficult to remove through image post-processing. The impact of lens flare on the recovered spectrum is highlighted in the bottom panel of Figure 8, where the spectra from pixels "A" and "C" are superposed. The intensity spectra from pixel "C" shows two small CO_2 spikes, as we would expect inside the plume but not outside the plume. It also shows an increase of intensity at 2,150 cm^{-1} corresponding to CO emission lines. From the spectra at pixel "C", it is difficult to identify that those spectral signatures come from an optical artifact and not from species emissions. This artifact will cause the CO and CO_2 column densities of these pixels to be over-estimated.

The "hole" between the red and blue CO_2 spikes for highlights the importance of accounting for the atmospheric layer between the flare plume and the camera in the spectroscopic model. Ambient conditions can often be inferred from the hyperspectral data by selecting pixels from the flare stack region. In this particular measurement, however, the stack pixels are strongly affected by the lens flare, so onsite concentrations of CO_2 and H_2O and temperature are used instead (Table 2). Given the long pathlength between the flare plume and the camera, it is crucial to include the $^{13}C^{16}O_2$ isotopologue, which has a natural abundance of approximately 1% and a red-shifted absorption spectrum compared to that of the main $^{12}C^{16}O_2$ isotopologue.

Table 2: Ambient conditions set for the combustor hyperspectral measurement

Parameter	Onsite measured values
CO_2	426 ppm[1]
H_2O	2914 ppm (RH = 44%)[1]
T_{amb} (K)	289 K[2]

[1]Picarro station
[2]Davis weather station

Figure 9 shows the column density profiles for of CO_2 and CO, inferred using Eq. (3), the plume temperature, as well as the velocity profile found from the Lucas-Kanade algorithm. Since there were no CH_4 features in the intensity spectra, a subregion of the detection spectrum, between 2000 and 2470 cm^{-1}, was used for the inference, and a blackbody spectrum corresponding to 255 K is assumed for the background.

During the field trial wind speed was approximately 2.5 m/s during the measurement period, which is in good agreement with the peak velocity inferred from the optical flow algorithm. The velocities and column densities along the control line are used to infer the species mass flow rate, Eq. (2), and then multiplied by their respective carbon mass ratios (CO_2: 12/44, CO: 12/28) to obtain the carbon mass flow rate and estimate the combustion efficiency via Eq. (1). Figure 9 shows that the column densities increase drastically outside the plume compared to their densities

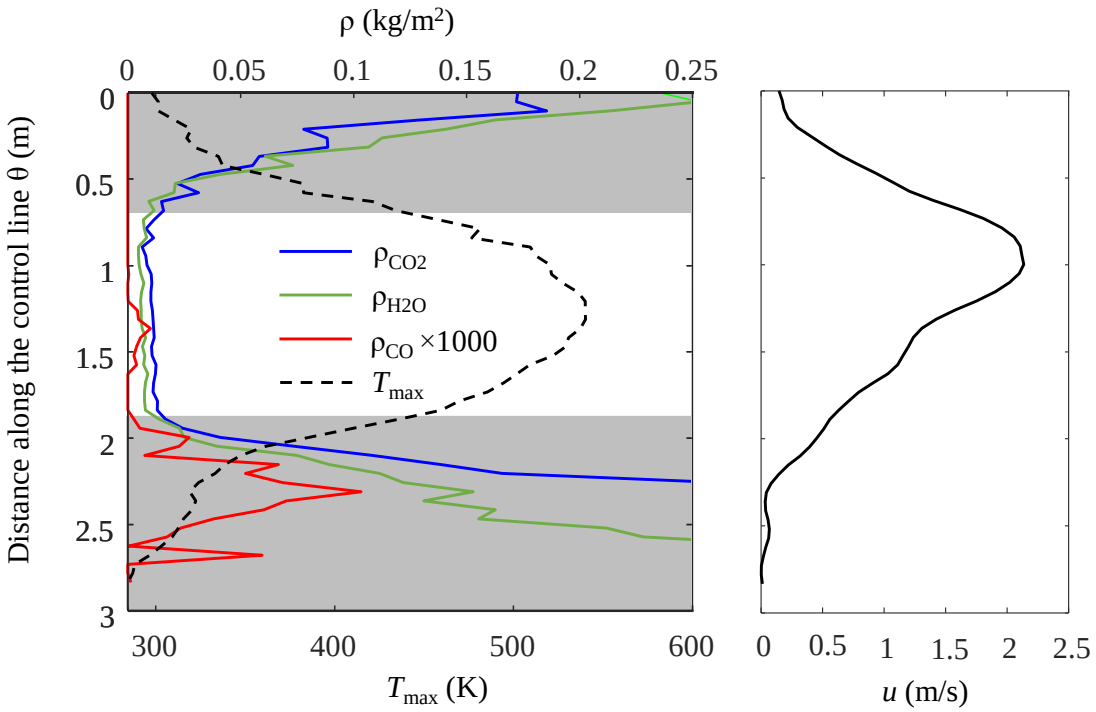

Figure 9: Column densities and peak temperature inferred from the spectroscopic model, and velocity profile inferred from the optical flow algorithm, for the combustor shown in Fig. 6. The shaded regions are excluded from the mass flow rate calculation.

inside the plume (0.7 m < θ < 1.9 m). This behaviour is caused by the lens flare effects depicted in Fig. 7 (b), and of the mischaracterization of the background intensity when modelled by Eq. (4). Quantification of the species mass flow rate and of combustion efficiency is therefore conducted only for pixels covering the plume. Results are summarized in Table 3. When only considering the part of the control line that crosses the plume (0.7 m < θ < 1.9 m), as labeled in Fig. 9, the combustor carbon mass flow rate is estimated at $\dot{m}_C$ = 5.8 g/s, which is in good agreement with the known natural gas input carbon mass flow rate of 6.1 g/s (42.5 SCM of natural gas per hour). This corresponds to a CE greater than 99%.

Table 3: CO_2 and CO mass flow rates of the combustor, inferred using the IFTS.

Species, k	$\dot{m}_{C,k}$ (g/s)
CO_2	5.8
CO	~ 0

5.3.IFTS measurement of a steam-assisted flare at a refinery

A key application for this technique lies in conducting fenceline measurements on flares that burn unknown fuel compositions and at unknown rates, as is the case of a steam-assist flare at a petrochemical refinery in Southern Ontario, shown in Fig. 10.

A 128 px ×128 px subdomain of the FPA was used to image the flare, which corresponds to a (22.4×22.4) m^2 area for a measurement distance of 580 m. The spectral resolution was set to 4 cm^{-1}. With these parameters and an integration time of 100 μs per image, the imaging framerate was 747 Hz, which required 3.17 s to form a complete interferogram. Figure 11 (*a*) shows the spectral intensity map for 2960 cm^{-1}, a part of the spectra that contains features corresponding to the principle C-H stretching mode of many hydrocarbons, while Figure 11 (*b*) shows the spectral

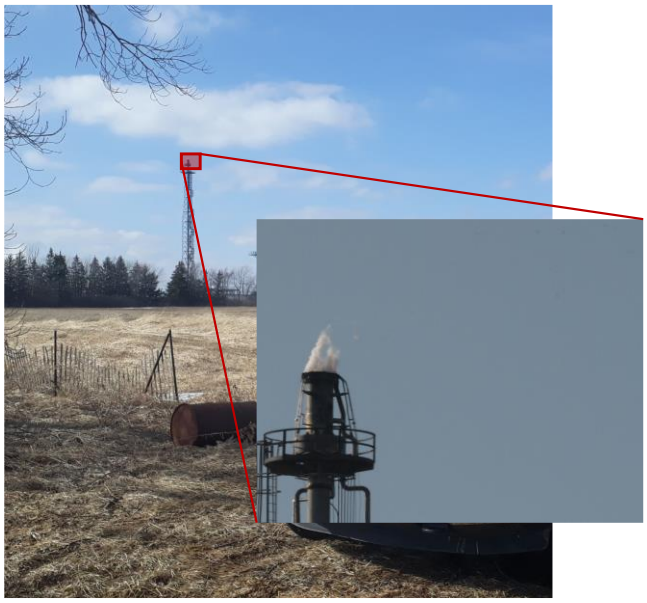

Figure 10: Steam assisted flare at a refinery. Measurements were carried out at a standoff distance of approximately 580 m.

intensity map for another wavenumber, $\eta = 2224$ cm^{-1}, corresponding to the combustion products CO and CO_2. For that wavenumber, the map illustrates the lense flare artefacts and the flare halo that affect the infrared image. As the lens flare transects the control line pixels, this artifact will interfere with the inversion procedure and the column densities estimates.

Figure 12 (*b*) shows the intensity spectra for pixels above and within the plume ("A", "B") and for a pixel at the plume extremity ("C"), along with absorption coefficients for H_2O, CO_2, and CO, all of which are expected to be in the flare plume. The intensity spectra indicate the presence of CO_2, H_2O, CO, while the feature between 2800-3000 cm^{-1} visible in the spectra for pixels "B" and "C" indicates the presence of an unknown hydrocarbon. In the case of flares used to dispose of process gas for upstream oil and gas production this signal would likely be CH_4, but the absence of the R-branch lines at higher wavenumbers indicates the presence of a heavier hydrocarbon. The

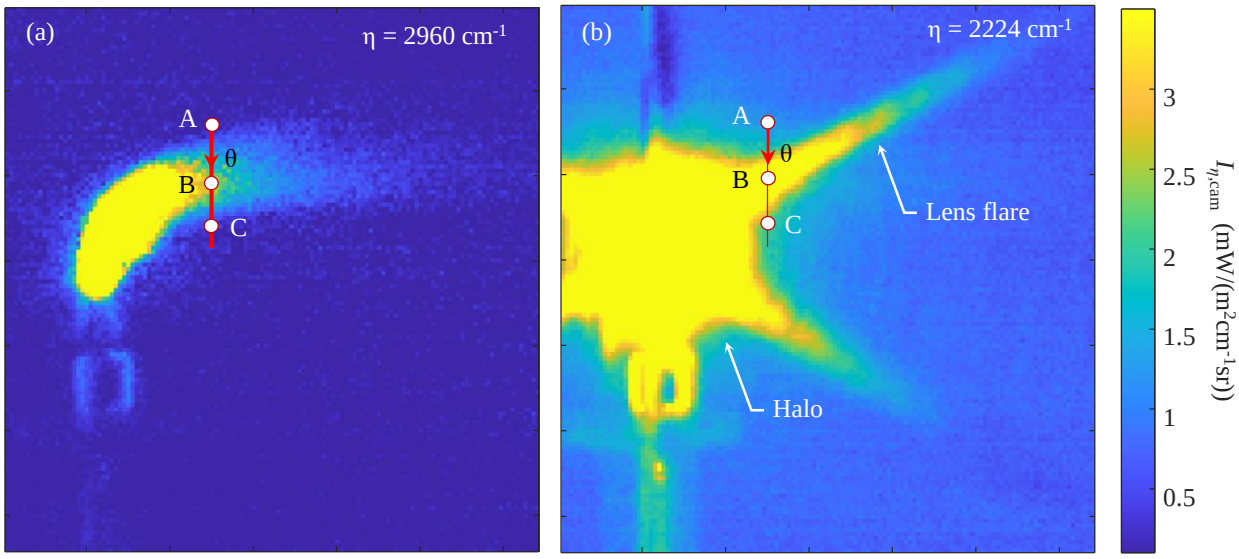

Figure 11: (a) Intensity map at 2224 cm^{-1} of the flare shown in Fig.10; this wavenumber corresponds to CO and CO_2 emission lines. For that wavenumber, lens flare and glowing of the flare is observed on the image. (b) Intensity map at 2960 cm^{-1} of the flare shown in Fig. 10; this wavenumber corresponds to the principle C-H stretching mode of hydrocarbons. The National Pollution Release Inventory suggests that the flare is likely burning butane, which is consistent with the detected spectra (Fig. 12 (b)).

National Pollutant Release Inventory for this facility [25] suggests that the HC is butane, C_4H_{10}. Like many heavier hydrocarbons, line parameters for butane are not available in the HITRAN database. Instead, a comparison of the experimentally-derived molecular absorption cross-section [20, 26] and the IFTS emissions spectrum confirms that this emission feature likely corresponds to butane. This empirically-derived absorption spectrum is incorporated into the spectroscopic model. This result highlights the importance of spectral and spatial resolution when calculating flare CE, particularly for downstream oil and gas operations since the absorption cross-sections of hydrocarbons generally do not scale with the number of carbons per molecule.

As mentioned for the combustor measurements, the spectra in Fig. 12 (*b*) corresponding to pixels “B” and “C” feature two CO_2 emission “spikes” caused by emission the hot CO_2 in the flare plume and its absorption by the ambient CO_2. For each pixel “A”, “B” and “C”, the spectra show

an increase in intensity around wavenumber 2224 cm^{-1} that correspond to the halo and lens flare artefacts. For pixels inside the plume like "B" and "C", the model attempt to recover that fictitious signal by an increase in the CO_2 concentration. In Figure 12 (*a*), are represented the column densities and plume maximum temperature along the control line. The CO_2 column density profile is increasing for pixels located at the plume extremities (e.g. pixel "C"), illustrating the effect of lens flare and the overcompensation of the model (spectra "C" in Fig. 12 (*b*)). The CO_2 and C_4H_{10} spikes at the control line top and bottom pixels can be explained by those artefacts but also by the mischaracterization of the background, as shown by the intensity spectrum "A" in Fig. 12 (*b*).

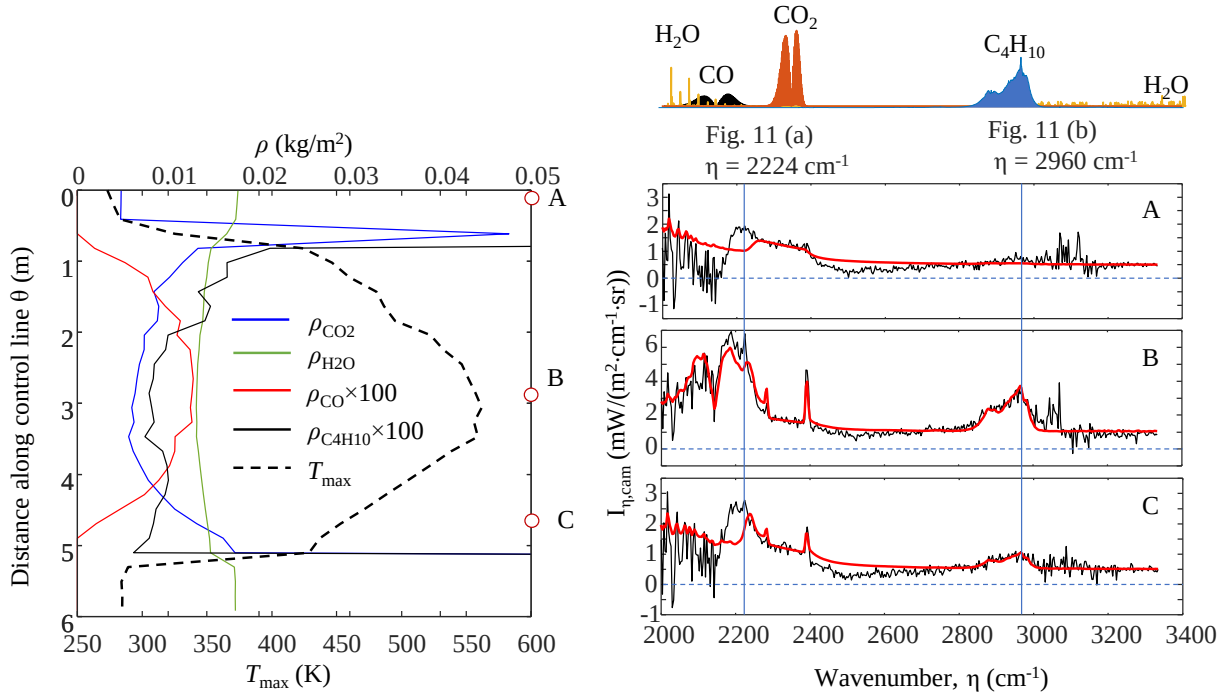

(a) (b)

Figure 12: (a) Column densities and peak temperature inferred along the control line shown in Fig. 11. The spikes in column density at the extreme ends of the integration line are likely caused by lens flare artifacts and mischaracterization of the background. The positions "A", "B" and "C" labeled along the control line correspond to the ones in Fig. 11; (b) Intensity spectra for pixels at positions "A", "B" and "C", along with the absorption coefficient of candidate species. Blue lines for wavenumbers corresponding to Fig. 11 images, show the emission from butane (η = 2960 cm^{-1}) as well as the lens flare and glowing effect on the spectra (η = 2224 cm^{-1}).

The ambient CO_2 and H_2O concentration and temperature needed to interpret the spectra are shown in Table 4. Apart from the background and lens artefact, the modeled spectra are in excellent agreement with the measured spectra.

Table 4: Ambient conditions during the hyperspectral measurement of the petrochemical flare.

Parameter	Value
CO_2	413 ppm[1]
H_2O	3666 ppm (RH = 60%[2])
T_{amb} (K)	280 K[3] (280.3 K[2])

[1]Based on average atmospheric abundance
[2]Environment Canada
[3]Onboard thermocouple

The velocities are found from the Lucas-Kanade algorithm, with a maximum normal velocity of 4.5 m/s. Column densities and velocities are substituted into Eq. (2) to obtain the mass flow rates shown in Table 5. Finally, these mass flow rates are multiplied by their respective carbon mass ratios (CO_2: 12/44, CO: 12/28, C_4H_{10}: 48/58) and then substituted into Eq. (1) to obtain an overall flare combustion efficiency of 97%.

Table 5: CO_2, CO, and C_4H_{10} carbon mass flow rates for the petrochemical flare.

Species, k	$\dot{m}_{C,k}$ (g/s)
CO_2	27.2
CO	0.5
C_4H_{10}	0.3

6. Conclusions and future work

This study presents a technique for estimating flare combustion efficiency using a MWIR HS camera. The mass flow rates needed for this calculation are found by combining species column densities inferred using a spectroscopic model with a 2D velocity field obtained using an optical

flow algorithm. Crucially, this technique provides the capacity to infer flow rates and flare efficiency through fenceline measurements, without requiring any knowledge about the fuel flow rate supplied to the flare. This tool may be used by operators, flare equipment manufacturers, and regulators to assess the combustion efficiency of flares *in situ* through standoff measurements. This information is crucial to understand and minimize the impact of flaring on climate change. While the approach focused on calculating CE, it may also be used to quantify emissions of other types of flare emissions, including black carbon [27] and sulphur dioxide [28]. The combined spectral and spatial resolution afforded by the IFTS is particularly well-suited in cases where the species may be distributed heterogeneously in the flare plume and in cases where the species present in the plume may be unknown or uncertain.

Despite the strong potential of this technique, there are a number of challenges that must be overcome in order to improve the reliability of this approach. First and foremost, it is necessary to quantify the uncertainties attached to the column densities and mass flow rates used to estimate the CE, and to carry out benchmark validation measurements using an independent measurement technique. The inversion of the spectroscopic model is deeply ill-posed, since an infinite set of concentration and temperature distributions exist that, when substituted into Eq. (4), could explain the spectroscopic data. The imposition of Gaussian profiles may be reasonable in a time-averaged sense, but the instantaneous intensity field may be influenced strongly by turbulent fluctuations between the concentration and temperature field (so-called “turbulence-radiation interactions” [29]). A second source of model error comes from the use of intensity-weighted projected velocities obtained from the optical flow algorithm. When the intensity variations are caused by the absorption of background radiation it can be shown that the projected velocity field is a “mass-weighted velocity”, which is appropriate for calculating a mass-flow rate [30, 27]. In this case,

however, the intensity variations are due to coupled fluctuations in local temperature and concentration, and the resulting velocity field may not be mass-weighted. In both regards, working with Bayesian inversion methods could help with both of those objectives, as it formalizes the inclusion of prior information and account for quantification of the measurement and model uncertainty propagation to the estimates.

There also remain several issues related to hardware implementation. Hyperspectral images of the combustor and petrochemical flares were contaminated with lens flare features, likely caused by coherent scattering of the most intense source of incident intensity (e.g., hot CO_2) by defects in the optics. These artifacts are difficult to remove since they contaminate the broadband images that are Fourier-transformed into the recovered spectra. Turbulence-induced SCAs and lens flare both impact the intensity spectrum, and therefore the inferred temperature and species column densities. While the impact of SCAs may be mitigated through filtering, flare artifacts are considerably more challenging to remove. Future work will focus on developing image processing techniques to remove lens flare, and experimental procedures for avoiding these features in the first place.

Data availability statement

The data that support the findings of this study are openly available in "Replication Data for: Quantifying Flare Combustion Efficiency using an Imaging Fourier Transform Spectrometer" at https://doi.org/10.5683/SP3/JLMYWE.

Acknowledgments

This research was sponsored by NSERC's FlareNet (NETGP 479641-15). The authors are grateful to Defence Research and Development Canada for providing their Imaging Fourier Transform Spectrometer.

References

[1] "World Bank, Global Gas Flaring Reduction Partnership (GGFR)," World Bank, [Online]. Available: https://www.worldbank.org/en/programs/gasflaringreduction/global-flaring-data. [Accessed July 2023].

[2] A. E. Aoun, V. Rasouli and Y. Khetib, "Assessment of Advanced Technologies to Capture Gas Flaring in North Dakota," *Arabian Journal for Science and Engineering*, p. 1–19, 2023.

[3] U. S. E. O. of Air Quality Planning and S. (OAQPS), "Parameters for Properly Designed and Operated Flares," 2012. [Online]. Available: https://www3.epa.gov/airtoxics/flare/2012flaretechreport.pdf.

[4] M. R. Johnson, D. J. Wilson and L. W. Kostiuk, "A fuel stripping mechanism for wake-stabilized jet diffusion flames in crossflow," *Combust. Sci. Technol.*, vol. 169, pp. 155-174, 2001.

[5] M. Zamani, E. Abbasi-Atibeh, S. Mobaseri, A. H., A. Ahsan, J. S. Olfert and L. W. Kostiuk, "An experimental study on the carbon conversion efficiency and emission indices of air and stream co-flow diffusion jet flames," *Fuel*, vol. 287, p. 119534, 2021.

[6] A. Ahsan, H. Ahsan, J. S. Olfert and L. W. Kostiuk, "Quantifying the carbon conversion efficiency and emission indices of a lab-scale natural gas flare with internal coflows of air or steam," *Experimental Thermal and Fluid Science,* vol. 103, p. 133–142, 2019.

[7] G. Plant, E. A. Kort, A. R. Brandt, Y. Chen, G. Fordice, A. M. Gorchov Negron, S. Schwietzke, M. Smith and D. Zavala-Araiza, "Inefficient and unlit natural gas flares both emit large quantities of methane," *Science,* vol. 377, p. 1566–1571, 2022.

[8] V. M. Torres, S. Herndon and D. T. Allen, "Industrial flare performance at low flow conditions. 2. Steam-and air-assisted flares," *Industrial & engineering chemistry research,* vol. 51, p. 12569–12576, 2012.

[9] D. R. Caulton, P. B. Shepson, M. O. L. Cambaliza, D. McCabe, E. Baum and B. H. Stirm, "Methane destruction efficiency of natural gas flares associated with shale formation wells," *Environmental science & technology,* vol. 48, p. 9548–9554, 2014.

[10] A. Gvakharia, E. A. Kort, A. Brandt, J. Peischl, T. B. Ryerson, J. P. Schwarz, M. L. Smith and C. Sweeney, "Methane, black carbon, and ethane emissions from natural gas flares in the Bakken Shale, North Dakota," *Environmental Science & Technology,* vol. 51, p. 5317–5325, 2017.

[11] J. Wormhoudt, S. C. Herndon, J. Franklin, E. C. Wood, B. Knighton, S. Evans, C. Laush, M. Sloss and R. Spellicy, "Comparison of remote sensing and extractive sampling measurements of flare combustion efficiency," *Industrial & engineering chemistry research,* vol. 51, p. 12621–12629, 2012.

[12] Y. Zeng, J. Morris and M. Dombrowski, "Validation of a new method for measuring and continuously monitoring the efficiency of industrial flares," *Journal of the Air & Waste Management Association*, vol. 66, p. 76–86, 2016.

[13] V. Farley, A. Vallières, M. Chamberland, A. Villemaire and J.-F. Legault, "Performance of the FIRST: a long-wave infrared hyperspectral imaging sensor," in *Optically Based Biological and Chemical Detection for Defence III*, 2006.

[14] K. C. Gross, K. C. Bradley and G. P. Perram, "Remote identification and quantification of industrial smokestack effluents via imaging Fourier-transform spectroscopy," *Environmental science & technology*, vol. 44, p. 9390–9397, 2010.

[15] P. Tremblay, K. C. Gross, V. Farley, M. Chamberland, A. Villemaire and G. P. Perram, "Understanding and overcoming scene-change artifacts in imaging Fourier-transform spectroscopy of turbulent jet engine exhaust," in *Imaging Spectrometry XIV*, 2009.

[16] S. Savary, J.-P. Gagnon, K. Gross, P. Tremblay, M. Chamberland and V. Farley, "Standoff identification and quantification of flare emissions using infrared hyperspectral imaging," in *Advanced Environmental, Chemical, and Biological Sensing Technologies VIII*, 2011.

[17] S. J. Grauer, B. M. Conrad, R. B. Miguel and K. J. Daun, "Gaussian model for emission rate measurement of heated plumes using hyperspectral data," *Journal of Quantitative Spectroscopy and Radiative Transfer*, vol. 206, p. 125–134, 2018.

[18] R. B. Miguel, S. Talebi-Moghaddam, M. Zamani, C. Turcotte and K. J. Daun, "Assessing flare combustion efficiency using imaging Fourier transform spectroscopy," *J. Quant. Spectrosc. Rad. Trans.*, vol. 273, p. 107835, 2021.

[19] J. H. Pohl, B. A. Tichenor, J. Lee and R. Payne, "Combustion efficiency of flares," *Combustion science and technology,* vol. 50, p. 217–231, 1986.

[20] I. E. Gordon, L. S. Rothman, R. J. H. R. Hargreaves, E. V. Karlovets, F. M. Skinner, E. K. Conway, C. Hill, R. V. Kochanov, Y. Tan, P. Wcisło, A. Finenko, K. Nelson, P. Bernath, M. Birk, V. Boudon, A. Campargue and K. Chance, "The HITRAN2020 molecular spectroscopic database," *J. Quant. Spectrosc. Radiat. Transf.,* vol. 277, p. 107949, 2022.

[21] H. E. Revercomb, H. Buijs, H. B. Howell, D. D. LaPorte, W. L. Smith and L. A. Sromovsky, "Radiometric calibration of IR Fourier transform spectrometers: solution to a problem with the High-Resolution Interferometer Sounder," *Applied Optics,* vol. 27, p. 3210–3218, 1988.

[22] MathWorks, "lsqnonlin documentation," MathWorks, 2023. [Online]. Available: https://www.mathworks.com/help/optim/ug/lsqnonlin.html. [Accessed 2023].

[23] B. K. P. Horn and B. G. Schunck, "Determining optical flow," *Artificial intelligence,* vol. 17, p. 185–203, 1981.

[24] B. D. Lucas and T. Kanade, "An iterative image registration technique with an application to stereo vision," in *IJCAI'81: 7th international joint conference on Artificial intelligence*, 1981.

[25] Government of Canada, "National Pollutant Release Inventory," [Online]. Available: https://www.canada.ca/en/services/environment/pollution-waste-management/national-pollutant-release-inventory.html. [Accessed 30 June 2022].

[26] S. W. Sharpe, T. J. Johnson, R. L. Sams, P. M. Chu, G. C. Rhoderick and P. A. Johnson, " "Gas-Phase Databases for Quantitative Infrared Spectroscopy", Applied Spectroscopy 58, 1452-1461 (2004)," *J. Quant. Spectrosc. Radiat. Trans.,* vol. 58, pp. 1452-1461, 2004.

[27] B. M. Conrad and M. R. Johnson, "An uncertainty-based protocol for the setup and measurement of soot-black carbon emissions from gas flares using sky-LOSA," *Atmos. Meas. Tech.,* vol. 14, p. 1573, 2021.

[28] M.-A. Gagnon, S. S. Tremblay, P. Lagueux and M. Chamberland, "Stanoff thermal hyperspectral imaging for flare and smokestack characterization in industrial environments," in *5th Workshop on Hyperspectral Image and Signal Processing: Evolution in Remote Sensing*, Gainesville, FL, 2013.

[29] A. Gupta, D. C. Haworth and M. F. Modest, "Turbulence-radiation interactions in large-eddy simulations of luminous and nonluminous nonpremixed flames," *Proc. Comb. Inst.,* vol. 34, pp. 1281-1288, 2013.

[30] A. Montazeri, X. Zhou and J. D. Albertson, "On the viability of video imaging in leak rate quantification: a theoretical error analysis," *Sensors,* vol. 21, p. 5683, 2021.

[31] R. DeÍPapa Moreira Scafutto, C. Robertode Souza Filho, D. N. Riley and W. Jose de Oliveira, "Evaluation of thermal infrared hyperspectral imagery for the detection of onshore methane plumes: Significance for hydrocarbon exploration and monitoring," *Int J Appl Earth,* vol. 64, pp. 311-325, 2018.

[32] G. of Canada, "National Pollutant Release Inventory," 2022. [Online]. Available: https://www.canada.ca/en/services/environment/pollution-waste-management/national-pollutant-release-inventory.html.

[33] J. L. Massman and K. C. Gross, "Understanding the influence of turbulence in imaging Fourier transform spectroscopy of smokestack plumes," in *Algorithms and Technologies for Multispectral, Hyperspectral, and Ultraspectral Imagery XVII*, 2011.

488

489

490

491